Low-Complexity Beamforming Design for Green Near-Field Communications in 6G Ultra-Massive Multiple-Input–Multiple-Output

Xin Wang, *Member, IEEE*, Jianhui Lv, *Member, IEEE*, Adam Slowik, *Senior Member, IEEE*, Byung-Gyu Kim, *Senior Member, IEEE*, B. D. Parameshachari, *Senior Member, IEEE*, and Keqin Li, *Fellow, IEEE*

***Abstract*—The ultra-massive multiple-input-multiple-output (UM-MIMO) is envisioned to be an integral part of future sixth-generation (6G) communication networks to meet the ever-increasing demand for higher data rates. However, the excessive energy consumption of UM-MIMO's massive radio frequency chains and performance degradation due to beam misalignment pose critical challenges. This paper investigates low-complexity beamforming optimizations with UM-MIMO for green near-field (NF) wireless communications. We first propose an adjustable orientation discontinuous reception (A-ODRX) mechanism merging the beam alignment state into long DRX cycles to reduce power consumption while preserving beamforming capabilities enabled by UM-MIMO's large aperture. The A-ODRX mechanism demonstrates provable robustness against beam misalignments through theoretical derivations. We designed a phase extraction zero-forcing (PE-ZF) aided hybrid beamforming architecture tailored for NF channels' spherical waveform effects to further overcome hardware constraints. Simulation results demonstrate that the proposed low-complexity beamforming design for the green NF wireless communication method outperforms benchmarks in terms of energy efficiency, achievable sum rate, rate scaling with users, resilience to NF mobility, and beamforming gain.**

***Index Terms*—Ultra-massive multiple-input-multiple-output, low-complexity beamforming, green near-field wireless communications, 6G.**

I. Introduction

THE AMBITIOUS vision for beyond 5G networks sets towering targets for sixth-generation (6G) wireless systems spanning peak data rates exceeding 1 Tbps, latency below 0.1 ms, connectivity density surpassing 10 million nodes per km^2, and nines of reliability [1], [2]. Realizing these performance objectives requires fundamental reengineering across every communication facet. The proliferation of new mmWave and Terahertz bands coupled with the adoption of ultra-massive multiple-input-multiple-output (UM-MIMO) antenna arrays constituting hundreds to thousands of elements facilitates the extraordinary beamforming gains necessary to make the daunting 6G vision a reality [3], [4], [5], [6]. By synthesizing transmit and receive signals into very high-resolution pencil beams, UM-MIMO delivers immense improvements in link budget, overcoming free-space path loss and absorption effects to enable reliable communication over wider bandwidths, longer distances, and higher frequencies [7]. Additionally, the spatial isolation achieved by such narrow beams allows extensive frequency reuse and multiplexing, enhancing area traffic capacity. However, practical implementation needs to conquer hardware constraints arising from the excessive radio frequency components. Hence, optimizing the power efficiency and beamforming architectures while guaranteeing scalability remains pivotal. By offering new antenna proximity access opportunities, UM-MIMO also expands the scope of near-field networking applications spanning extended reality, connected healthcare, Industry 4.0 automation, etc. Substantially more interdisciplinary research is vital for unveiling the full potential of UM-MIMO in catalyzing next-generation wireless innovations across the 6G landscape.

However, harnessing the complete potential of UM-MIMO, especially extremely large-scale antenna arrays at such gigantic scales, for sustainable operation remains an open challenge. First, the excessive hardware complexity of dedicated baseband processing chains for each antenna becomes practically infeasible from affordability and power consumption perspectives. Hybrid architectures with drastically fewer RF modules aid affordability but sacrifice optimality. Then, the highly directional beams make reliably maintaining alignment quite difficult under mobility, causing frequent link failures and throughput drops [8]. While sophisticated beam tracking methods dynamically adjust directions, they impose substantial computational and signaling overheads, thus diminishing energy efficiency [9], [10]. UM-MIMO also necessitates rethinking channel modeling itself – the sheer scale of arrays gives rise to considerably expanded near-field (NF)

Manuscript received 15 January 2024; revised 13 May 2024; accepted 15 June 2024. Date of publication 20 June 2024; date of current version 17 February 2025. This work was supported by the National Natural Science Foundation of China under Grant 62202247. *(Corresponding author: Jianhui Lv.)*

Xin Wang is with the School of Information Science and Engineering, Northeastern University, Shenyang 110819, China.

Jianhui Lv is with the Department of Network, Peng Cheng Laboratory, Shenzhen 518057, China (e-mail: lvjh@pcl.ac.cn).

Adam Slowik is with the Department of Electronics and Computer Science, Koszalin University of Technology, 98701 Koszalin, Poland.

Byung-Gyu Kim is with the Division of Artificial Intelligence Engineering, Sookmyung Women's University, Seoul 04310, Republic of Korea.

B. D. Parameshachari is with the Department of Electronics and Communication Engineering, Nitte Meenakshi Institute of Technology, Bengaluru 560064, India.

Keqin Li is with the Department of Computer Science, State University of New York at New Paltz, New Paltz, NY 12561 USA.

Digital Object Identifier 10.1109/TGCN.2024.3416904

regions compared to conventional MIMO [11], [12], [13]. The resultant non-planar spherical wavefront induces phase distortions that traditional beamforming strategies designed for planar waveform operation fail to tackle, causing severe performance degradation. Overcoming hardware constraints through energy-efficient robust designs compatible with mobility and spherical propagations is pivotal. Despite the abundant promises, UM-MIMO still poses multifaceted optimization challenges. Holistic solutions call for cross-layer innovations spanning antenna theory, signal processing, communication algorithms, networking protocols, etc. Substantial interdisciplinary research across architecture, circuits, electromagnetics, communications, and networking is vital for sustainably harnessing UM-MIMO's potential at global scales.

While prior works have attempted to address subsets of the above multi-faceted challenges in the context of large, intelligent arrays and MIMO systems, a holistic approach combining all factors affecting sustainability, reliability, and adoption feasibility for massive array deployments in the 6G landscape remains lacking [14], [15], [16], [17]. For instance, energy-focused improvements to discontinuous reception designs are investigated in [18] and [19], and accurate near-field channel modeling methods are proposed in [20] and [21]. However, a joint examination of scalable architectures tackling hardware constraints, robust beamforming and alignment techniques counteracting mobility, adaptable baseband processing matching propagation environments, configurable medium access protocols, electromagnetic radiation hazard assessments, etc., needs completion [22], [23], [24], [25], [26]. As each aspect sees isolated improvements, consolidating cross-layer innovations spanning theory, algorithms, and practical considerations into a unified system-level framework is pivotal. All the modules must coordinate by applying complementary optimizations targeting the overarching goal of unlocking the abundant promises of UM-MIMO globally. A tremendous potential exists in exploring integrative research directions by combining multi-disciplinary expertise for sustainable and responsible 6G wireless networking evolution.

Against this backdrop, we propose an optimized green beamforming strategy named phase extraction zero-forcing (PE-ZF) that holistically addresses energy efficiency, mobility resilience, and low hardware complexity for NF UM-MIMO networks in 6G wireless systems, which is enabled via the following key contributions:

- Novel adjustable DRX mechanism with integrated beam tracking achieving excellent tradeoff between power saving and robust alignment.
- Efficient PE-ZF hybrid beamforming minimizing hardware requirements while cancelling inter-beam interference for reliable communications.
- Extensive simulations of proposed schemes substantiating significant joint enhancements across vital evaluation metrics over competitive baselines.

The remainder of this paper is organized as follows. The proposed adjustable orientation discontinuous reception (A-ODRX) scheme and PE-ZF hybrid beamforming strategy are elaborated in Sections II and III, respectively. Comprehensive performance evaluation results and associated insights are analyzed in Section IV. Finally, concluding remarks are provided in Section V, highlighting promising research directions.

II. System Model

In this section, we first formulate an accurate NF channel representation. We propose the green communication-oriented A-ODRX mechanism based on the derived NF model and establish the corresponding state transition model.

A. Preliminaries of NF Channel Characteristics

As depicted in Fig. 1, we consider a single-cell extremely large-scale antenna array downlink communication system operating over bandwidth B. The base station (BS) is equipped with N_t antennas and N_{RF} ($N_{RF} \leq N_t$) RF chains serving K single-antenna users randomly distributed in the same sector.

Fig. 1 depicts a single-cell downlink communication system where a base station equipped with a UM-MIMO antenna array serves multiple single-antenna users. The users are distributed across the NF and far-field regions relative to the base station. In the NF region, which is determined by the Rayleigh distance, the spherical wavefront characteristics of the propagating signals become prominent, leading to channel non-stationarities across the antenna array that traditional far-field assumptions fail to capture. On the other hand, users located in the far-field experience planar wavefronts, simplifying channel modeling. The proposed communication system aims to optimize beamforming strategies to cater to the distinct propagation phenomena in these two regions while maximizing energy efficiency.

Depending on the signal source (BS arrays) to the receiver (user) distance compared to the Rayleigh distance [27]:

$$Z = \frac{2D^2}{\lambda} \tag{1}$$

where D denotes the BS antenna array aperture and λ is the signal wavelength, the channel propagation can be classified as far-field or NF. Specifically, when users are located much farther than Z (e.g., cell edge), the impinging signals can be approximated with planar wavefronts. The far-field array response vector for uniform linear arrays is thus expressed as [28]:

$$\mathbf{a}(\theta) = \left[1, e^{j\pi \sin(\theta)}, \ldots, e^{j\pi(N_t-1)\sin(\theta)}\right]^T \tag{2}$$

where θ denotes the angle of departure (AoD).

However, for users moving within proximity to the BS (e.g., cell center), the emitted electromagnetic waves exhibit spherical waveform effects, necessitating accurate modeling using spherical wave array response:

$$\mathbf{b}(r,\theta) = \frac{r}{r_1} e^{-j\frac{2\pi(r_1-r)}{\lambda}} \ldots \frac{r}{r_{N_t}} e^{-j\frac{2\pi\left(r_{N_t}-r\right)}{\lambda}} \tag{3}$$

where r represents the distance between BS center and user, r_n denotes the distance between the nth BS antenna to user position. Unlike Eq. (2), which only depends on θ, and $\mathbf{b}(r,\theta)$ relates to both angular and range domains as highlighted by the $r_{1:N_t}$ terms. Such phenomena become increasingly prominent

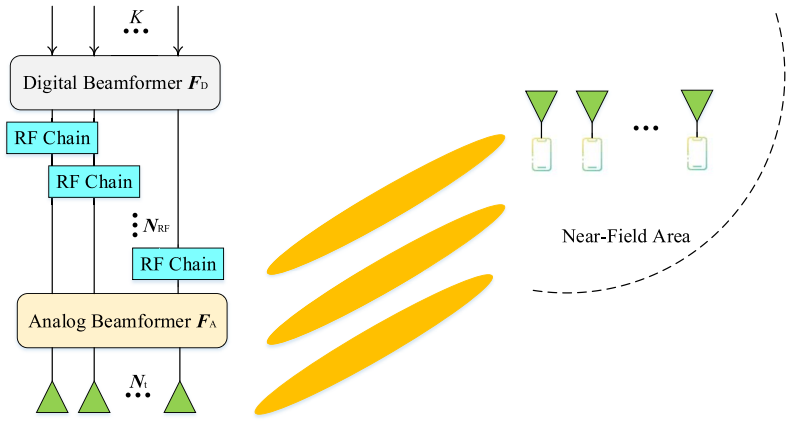

Fig. 1. Illustration of the UM-MIMO downlink communication system involving both NF and far-field user locations.

for UM-MIMO due to their enlarged aperture, rendering prior far-field planar wave assumptions invalid.

To quantify the resulting performance degradation, we define the power gain loss when directly applying far-field vectors in the NF as:

$$L = 1 - \frac{|\mathbf{a}^H(\theta)\mathbf{b}(r,\theta)|^2}{||\mathbf{b}(r,\theta)||^2} \tag{4}$$

Assuming the minor amplitude fluctuations among elements in $\mathbf{b}(r,\theta)$ to be negligible, we get:

$$\left|\mathbf{b}^H(r,\theta)\mathbf{b}(r,\theta)\right| \approx N \tag{5}$$

Further by applying Fresnel approximations [29] for quadratic phase terms when $r \gg \delta_n d$, the mismatch loss expression reduces to:

$$L \approx 1 - \frac{1}{N}\left|\sum_{n=0}^{N-1} e^{-j\pi \frac{\delta_n^2 \cos_2 \theta}{\lambda r}}\right|^2 \tag{6}$$

where $\delta_n = \frac{2n-(N-1)}{2}$.

Consider the downlink of a communication system where a UM-MIMO BS with N_T antenna elements and $N_{RF} = K$ RF chains serve K distributed single antenna users present in the BS NF.

Let the received signal vector across users be denoted by $\mathbf{y} \in \mathbb{C}^{K\times 1}$:

$$\mathbf{y} = \mathrm{HFs} + \mathbf{n} \tag{7}$$

where channel matrix $\mathbf{H} \in \mathbb{C}^{K\times N_T}$ represents propagation links between the BS and users. Transmit signal vector is $\mathbf{s} \sim \mathcal{CN}(\mathbf{0}, \mathbf{I})$ while $\mathbf{F} = \mathbf{F}_{RF}\mathbf{F}_{BB} \in \mathbb{C}^{N_T\times K}$ denotes the beamforming matrix with $\mathbf{F}_{RF}$ and $\mathbf{F}_{BB}$ being analog and digital beamforming matrices respectively. Additive noise is $\mathbf{n} \sim \mathcal{CN}(\mathbf{0}, \sigma^2\mathbf{I})$.

When accurate NF effects are modeled using the spherical wavefront formulation, the channel between BS and the kth user is:

$$\mathbf{h}k^{nf} = \alpha_0 \mathbf{b}(r_0,\theta_0) + \frac{1}{P}\sum_{p=1}^{P} \alpha_p \mathbf{b}(r_p,\theta_p) \tag{8}$$

where α_0 and $\mathbf{b}(r_0,\theta_0)$ represent the line-of-sight (LoS) path gain and array response focused toward the LoS path angle of arrival θ_0 and user range r_0, respectively. Likewise, α_p and $\mathbf{b}(r_p,\theta_p)$ denote the channel gain and array response corresponding to the pth non-line-of-sight (NLoS) path arriving from (θ_p, r_p).

In contrast, simplistic far-field approximation relies on planar wavefronts instead of actual spherical profiles, leading to substantial performance loss:

$$\mathbf{h}k^{ff} = \alpha_0 \mathbf{a}(\theta_0) + \frac{1}{P}\sum_{p=1}^{P} \alpha_p \mathbf{a}(\theta_p) \tag{9}$$

The achievable system sum rate R quantifies the holistic spectral efficiency:

$$R = \sum_{k=1}^{K} R_k = \sum_{k=1}^{K} \log_2\left(1 + \frac{|\mathbf{h}_k\mathbf{f}_k|^2}{\sum i=1, i\neq k^K |\mathbf{h}_k\mathbf{f}_i|^2 + \sigma^2}\right) \tag{10}$$

where $\mathbf{f}_k$ represents the beamforming precoder for kth user. We deliberately adopt the inherent NF channel $\mathbf{h}_k$ when calculating R for fairness, although BS may use far-field estimates under unrealistic planar wave assumptions.

The presented UM-MIMO NF signal, channel, and system models lay the foundation for accurately analyzing spherical wave propagation physics and designing high-performance communication strategies tailored for 6G.

B. A-ODRX Mechanism

Continuously keeping active RF circuits undoubtedly allows for optimal beam alignment, but doing so incurs significant energy waste. A natural approach is dynamically adjusting RF activation levels according to traffic variations. In this regard, we propose the A-ODRX mechanism customized for NF UM-MIMO channels by merging beam alignment procedures into existing long DRX cycles.

1) State Transition Model: The state transitions in A-ODRX follow a semi-Markov model involving alternating active and dormant states, illustrated in Fig. 2.

Let T_{IN}, T_{ON}, T_{SC}, and T_{LC} denote the inactivity timer, ON duration timer, short DRX cycle, and long DRX cycle

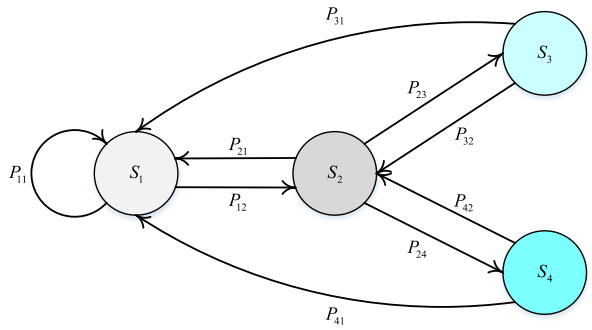

Fig. 2. State transition model of the proposed A-ODRX mechanism.

respectively. The duration timer and long DRX cycle, respectively. The UE resides in the following states:

- Active (S1): Uplink/downlink data communications take place. UE monitors the physical downlink control channel (PDCCH) and resets T_{IN} after packet arrival.
- Short DRX Sleep (S2): UE enters after T_{IN} expiration without triggering packets. It skips PDCCH monitoring, but RF remains active.
- Long DRX Sleep with Beam Scanning (S3): UE periodically measures reference signals across all beam pairs between next Generation Node B and itself. It feeds back the best beam once identified and synchronized. The long sleep period T'_{LC} adapts to traffic variations:

$$T'_{\mathrm{LC}} = \begin{cases} (2^{\alpha})^{i-1} T_{\mathrm{LC,min}} & (2^{\alpha})^{i-1} T_{\mathrm{LC,min}} \leq T_{\mathrm{LC,max}} \\ T_{\mathrm{LC,max}} & \text{otherwise} \end{cases} \tag{11}$$

where *i* denotes the *i* th entry to the current long DRX cycle, $\alpha \geq 0.5$ governs the long sleep period increment ratio.

The key novelty lies in the amalgamated design of beam scaning functionalities into existing long DRX cycles (S3), which opportunistically corrects beam misalignments only during off-peak traffic loads. This overcomes alignment outage problems faced in legacy DRX designs while avoiding dedicated beam training overheads. The long sleep period T'_{LC} adaption further exploits traffic burstiness for enhanced energy savings.

Based on the operation of the A-ODRX mechanism, we establish the mathematical state transition model characterized by the transition probability matrix $\mathbf{P}$. Let $p_{i,j}$ denote the transition probability from state S_i to S_j:

- $S_1 \rightarrow S_1$: Packet arrival before T_{IN} expiration resets inactivity timer. Hence:

$$p_{1,1} = p_{os}\left(1 - e^{-\lambda_{pc} T_{\mathrm{IN}}}\right) + p_{ns}\left(1 - e^{-\lambda_s T_{\mathrm{IN}}}\right) \tag{12}$$

- $S_1 \rightarrow S_2$: Transition occurs when T_{IN} expires without packet triggering:

$$p_{1,2} = 1 - p_{1,1} \tag{13}$$

- $S_2 \rightarrow S_3$: Transition after T_{ON} expiration without packet arrival:

$$p_{2,3} = p_{os}\left(1 - e^{-\lambda_{pc} T_{\mathrm{ON}}}\right)\left[1 - e^{-\lambda_{pc} N_{\mathrm{SC}} T_{\mathrm{SC}}}\right] + p_{ns} e^{-\lambda_s T_{\mathrm{ON}}}\left[1 - e^{-\lambda_s N_{\mathrm{SC}} T_{\mathrm{SC}}}\right] \tag{14}$$

- $S_2 \rightarrow S_4$: Transition when short cycle counter N_{SC} expires:

$$p_{2,4} = p_{os} e^{-\lambda_{pc} T_{\mathrm{ON}}} e^{-\lambda_{pc} N_{\mathrm{SC}} T_{\mathrm{SC}}} + p_{ns} e^{-\lambda_s T_{\mathrm{ON}}} e^{-\lambda_s N_{\mathrm{SC}} T_{\mathrm{SC}}} \tag{15}$$

- $S_3 \rightarrow S_1$: New packet arrival when UE briefly awakens for PDCCH monitoring:

$$p_{3,1} = p_{os}\left(1 - e^{-\lambda_{pc} T_{\mathrm{SS}}}\right) + p_{ns}\left(1 - e^{-\lambda_s T_{\mathrm{SS}}}\right) \tag{16}$$

where $T_{\mathrm{SS}} = T_{\mathrm{SC}} - T_{\mathrm{ON}}$ represents the short sleep period.

- $S_3 \rightarrow S_2$: No packets detected during PDCCH monitoring interval:

$$p_{3,2} = p_{os} e^{-\lambda_{pc} T_{\mathrm{SS}}} + p_{ns} e^{-\lambda_s T_{\mathrm{SS}}} \tag{17}$$

- $S_4 \rightarrow S_1$: Same as $S_3 \rightarrow S_1$ transition where T_{SS} gets replaced by dynamic long sleep period T'_{LC}.
- $S_4 \rightarrow S_2$: Same as $S_3 \rightarrow S_2$ but with updated T'_{LC} parameter.

By further defining state residence time vector $\Theta = [\theta_1, \theta_2, \theta_3, \theta_4]$, the average DRX incurred packet buffer delay can be derived as:

$$\delta_{\mathrm{DRX}} = \sum_{i=1}^{4} P(S_i)\delta_i = P(S_3)\delta_3 + P(S_4)\delta_4 \tag{18}$$

where $P(S_i)$ denotes the steady state probability of residing in state S_i, δ_i represents the average packet delay at state S_i. Specifically, $\delta_1 = \delta_2 = 0$ since UE continuously monitors PDCCH for incoming packets. For short, DRX state S_3 is defined as follows:

$$\delta_3 = T_{\mathrm{SS}} - \frac{p_{os}}{\lambda_{pc}}\left(1 - e^{-\lambda_{pc} T_{\mathrm{SS}}}\right) - \frac{p_{ns}}{\lambda_s}\left(1 - e^{-\lambda_s T_{\mathrm{SS}}}\right) \tag{19}$$

The rationale is that any packets arriving within interval T_{SS} need to wait for the next PDCCH monitoring instance to be served, contributing to the buffer delay. While for extended DRX state S_4:

$$\delta_4 = T'_{\mathrm{LC}} - \frac{pos}{\lambda_{pc}}\left(1 - e^{-\lambda_{pc} T' \mathrm{LC}}\right) - \frac{pns}{\lambda_s}\left(1 - e^{-\lambda_s T'_{\mathrm{LC}}}\right) \tag{20}$$

To quantify the energy savings yielded by the A-ODRX mechanism, we introduce the power-saving factor:

$$\Phi = \frac{P(S_3)\theta_3 + P(S_4)\theta_4}{\sum_{i=1}^{r} P(S_i)\theta_i} \tag{21}$$

where only states S_3 and S_4 correspond to UE sleep mode. Higher Φ indicates greater energy reduction.

2) Energy Savings Metric: The long-term proportion of sleep duration quantifies the energy benefits. Letting state S_i duration be θ_i with mean $E[\theta_i]$, the overall power savings factor is:

$$\eta = \frac{\sum_{i=3}^{4} P(S_i) E[\theta_i]}{\sum_{i=1}^{4} P(S_i) E[\theta_i]} \tag{22}$$

where $P(S_i)$ is probability of dwelling in state S_i obtained from transition matrix P_T and sleeping only occurs in states S_3 and S_4. $E[\theta_i]$ can be evaluated as:

$$E[\theta_i] = \overline{N}_{pc} \frac{1}{\lambda_p + P_{ns}\lambda_s[1-\exp(-\lambda_s t_i)] + P_{os}\lambda_{pc}[1-\exp(-\lambda_{pc} t_i)]} \tag{23}$$

where $\overline{N}_{pc}$ is mean packets per call and t_i denotes duration spend in state S_i. Higher incremental sleep expansion coefficient values α allow more aggressive dormancy for greater power efficiency.

The accuracy of beam pointing critically impacts connection stability. Letting the beam width be θ, user displacement velocity as ν and DRX sleep duration T_s, the misalignment probability in a short cycle is:

$$P_{sa} = \frac{1}{d}\int_{d}^{1+\nu T_s \tan\left(\frac{\theta}{2}\right)} dx \tag{24}$$

where d represents the link distance. The expression for long cycle P_{la} is similar with T_s replaced by the corresponding long sleep duration. $P_{sa},\ P_{la} \to 0$ denotes perfect alignment. Comparing these metrics across different beamforming strategies quantifies relative robustness.

The total latency comprises of beam search delay for alignment T_d and queuing delay δ:

$$T_L = T_d + \delta \tag{25}$$

where δ considers packets arrival rate λ during DRX cycle interval T_{CYC}:

$$\delta = T_{CYC} - \frac{1 - e^{-\lambda T_{CYC}}}{\lambda} \tag{26}$$

T_L should be constrained as per use case requirements. A complex tradeoff exists between T_L and energy savings metric η that the A-ODRX mechanism optimizes by balancing beam search overhead and sleep duration.

In summary, in conjunction with the proposed adjustable DRX sleep strategy, the semi-Markov modeling strikes an excellent balance between alignment reliability and energy optimization for mobile users situated in the NF of UM-MIMO.

III. Low-Complexity Beamforming Design for Green NF Communications

While the amalgamated A-ODRX mechanism reduces power consumption from the discontinuous reception perspective, designing suitable beamforming solutions catered to NF channels remains critical for optimizing system throughput and energy efficiency. However, directly translating conventional designs to the NF regime can risk suboptimality.

A. Challenges in Existing Beamforming Approaches

Legacy beamforming methods designed for far-field conditions face two main limitations regarding complexity and model mismatch when applied to UM-MIMO-aided NF communications: excessive complexity for large antenna arrays and model mismatch under NF conditions.

For a fully digital beamforming structure, the access point needs to dedicate one separate RF chain for each antenna element, leading to prohibitive energy and hardware overhead that scale linearly with array size:

$$P_{\text{dig}} = N_t(P_{\text{RFC}} + P_{BB} + P_{\text{CE}}) \tag{27}$$

where P_{RFC}, P_{BB}, and P_{CE} denote the power consumption of each RF chain, baseband processing unit, and channel estimation module respectively.

Although optimal in capacity performance, the sheer power usage and hardware costs become unaffordable for UM-MIMO with excessively large N_t. For instance, selecting $N_t = 2^{12} = 4096$ antennas at sub-THz bands for indoor applications can quickly amount to a kilo-watts level power budget, contradicting the green communication objectives.

Conventional beamforming designs predominantly assume planar wavefront channels as per Eq. (2), which can lead to significant performance deterioration when directly applied to NF scenarios due to multiple reasons:

- Power gain loss: As quantified in Eq. (28), reusing far-field codebooks under NF incurs considerable beamforming gain losses, translating to reduced receive SNR. Such losses intensify with closer user proximity and exacerbate dense deployments.

$$L \approx 1 - \frac{1}{N^2}\left(2N + 8\sum_{i=0}^{\frac{N}{2}-2}\sum_{j=1,j>i}^{\frac{N}{2}-1}\cos\left(\frac{\pi\cos_2\theta\left(W_{i,j}\right)}{\lambda \mathrm{r}}\right)\right) \tag{28}$$

- Inferior spatial resolution: Reusing far-field codebooks can inflate nominal beamwidth by over three times for the investigated scenario. The widened beams struggle to differentiate same-angle interference, causing severe inter-user interference.
- Range ambiguity: With planar wavefront assumption, radiated signals only differ in their angle of arrival, rendering beams incapable of distinguishing users at identical angles but different ranges, further hampering interference suppression.

Based on our evaluations, the joint impact of the above effects can lead to over 70% capacity reduction for cell-center users, highlighting the need for customized beamforming considering NF effects.

B. Proposed PE-ZF Hybrid Beamforming

Given the above complexity and mismatch issues, an attractive option lies in hybrid beamforming architectures realizing configurable trade-offs between performance and hardware costs. We detail the rationale and working principles behind the proposed PE-ZF hybrid beamforming for green NF wireless communications [30]. As depicted in Fig. 3, hybrid structure employs a low-dimensional digital baseband precoder $\mathbf{F}_{BB} \in \mathbb{C}^{N_{RF}\times K}$ in tandem with an analog RF precoder $\mathbf{F}_{RF} \in \mathbb{C}^{N_t \times N_{RF}}$ interfacing antennas, where $N_{RF} \ll N_t$ denotes the number of RF chains.

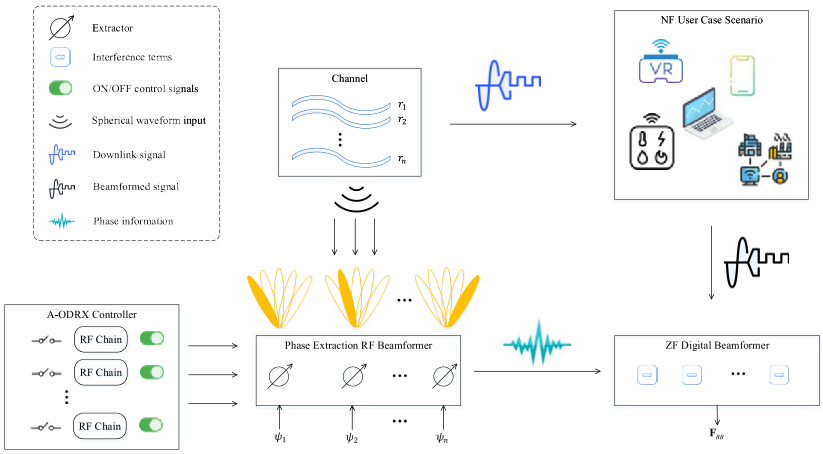

Fig. 3. Illustration of the proposed PE-ZF hybrid beamforming structure.

By condensing expensive hardware components into fewer RF paths, hybrid beamforming substantially curtails energy expenditures compared to complete digital solutions:

$$P_{\text{hyb}} = N_{RF}\left(P_{\text{RFC}} + P_{BB} + \frac{1}{N_t}P_{\text{CE}}\right) + N_t P_{PS} \quad (29)$$

where P_{PS} represents the power consumption of analog phase shifters. For exemplary parameter settings, P_{hyb} merely amounts to 24% of fully digital counterpart P_{dig}. Channel estimation complexity also reduces since only a dimension-reduced effective channel $\mathbf{H}_{\text{eff}} = \mathbf{H}\mathbf{F}_{RF}$ needs to be obtained. Besides complexity savings, hybrid architecture fits naturally with UM-MIMO NF channels by isolating and adapting to their unique propagation characteristics.

Instead of estimating full channel matrices, the analog beamformer condenses channel directionality information by extracting each user's phase response:

$$\mathbf{F}_{RF,k} = \frac{1}{\sqrt{N_t}}\mathbf{a}(r_k,\theta_k), \mathbf{a}(r_k,\theta_k) = e^{j\angle(\mathbf{h}k)} \quad (30)$$

where $\mathbf{h}_k = [h_{k,1}, h_{k,2}, \ldots, h_{k,N_t}]^T$ represents the kth user's channel vector. Unlike existing angle-only extraction methods, the joint (angle, range) domain phase extraction improves user differentiation by probing signals' multipath characteristics. RF phase shifter implementation also perfectly matches the constant modulus constraint in Eq. (30) without quantization errors.

With RF beamformer filtering out channel phase distortions, only $N_{RF} \times K$ baseband effective channel $\mathbf{H}_{\text{eff}} = \mathbf{H}\mathbf{F}_{RF}$ needs to be estimated.

The ZF digital beamformer, therefore, eliminates inter-user interference via pseudo inverse:

$$\mathbf{F}_{BB} = \beta\left(\mathbf{H}_{\text{eff}}^H\mathbf{H}_{\text{eff}}\right)^{-1} \quad (31)$$

where β denotes the power normalization factor, the cascaded RF-baseband structure decomposes UM-MIMO NF channels' spherical waveform effects and tackles them individually, achieving flexible performance-complexity trade-offs.

C. Asymptotic Capacity Analysis

We analyze the asymptotic capacity of the system under the proposed PE-ZF beamforming design. Assuming perfect channel state information at the transmitter, the received signal model is given as follows:

$$\mathbf{y} = (\mathbf{H}\mathbf{F}_{RF})\mathbf{F}_{BB}\mathbf{s} + \mathbf{n} \quad (32)$$

where $\mathbf{s}$ denotes transmitted symbol vector and $\mathbf{n}$ represents additive white Gaussian noise. Invoking vector approximation lemma in UM-MIMO regime $N_t \to \infty$, we have:

$$\mathbf{H}\mathbf{F}_{RF} \approx \mathbf{\Lambda} \quad (33)$$

where $\mathbf{\Lambda} = \text{diag}(\beta_1, \beta_2, \ldots, \beta_K)$ contains channel attenuation coefficients between selected beamforming direction and users with $\beta_k = \sqrt{N_t}\mathbf{h}_k^H\mathbf{F}_{RF,k}$. Substituting RF phase extraction design in Eq. (30), it follows that:

$$\beta_k = N_t, \forall k = 1, 2, \ldots, K \quad (34)$$

Aligning the RF beamformer with the users' channel phase response realizes constructive combining for signal power boost without leakage. With $\mathbf{F}_{BB}$ canceling inter-user interference via ZF and continuous amplitude scaling, the asymptotic capacity bound is thus derived as:

$$R^{\infty} = \lim_{N_t\to\infty} \det\left(\mathbf{I} + \rho\text{HF}\mathbf{F}^H\mathbf{H}^H\right) = K\left(1 + \rho N_t\right) \quad (35)$$

where ρ denotes transmit SNR. Observing the linear capacity scaling with N_t, Eq. (35) validates that the proposed PE-ZF Hybrid beamforming realizes the maximally achievable DoF offered by UM-MIMO and provides concrete theoretical grounds for its optimality besides empirical evidence.

D. Computational Complexity Analysis

We quantitatively analyze complexity by counting floating point operations. Without generality, we ignore common operations across schemes like channel estimation.

Consider K users, for the proposed PE-ZF method, phase extraction requires KN_T operations while $ZF = \mathcal{O}(K^3)$ assuming favorable channel conditions. So overall is $\mathcal{O}(KN_T + K^3)$.

PE-ZF has significantly lower complexity that crucially scales gracefully with antenna array size N_T, facilitating deployability for UM-MIMO regimes with reduced computing hardware specs and associated power drain.

In summary, the proposed PE-ZF architecture perfectly balances performance and implementation costs while catering accurately to UM-MIMO NF channel characteristics and facilitating sustainable green operations.

Subsequently, we analyze the impact of adopting PE-ZF hybrid beamforming architecture on pertinent performance metrics:

- Power Savings. Replacing a substantial chunk of high power-hungry RF chains with frugal phase shifters and combiners slashes overall power expenditure without severely affecting link reliability, enhancing system energy efficiency. Exact savings depend on configuration parameters.
- Latency. The acceleration of critical matrix algebraic modules using specialized hardware like tensor processing units combined with algorithm-architecture co-optimization ensures real-time operation essential for mobility and stringent delay demands.
- Hardware Requirements. PE-ZF allows modulo-2π phase control using low-resolution phase shifters that are cheaper, more robust, and power efficient, unlike high precision expensive components necessitated for complete digital solutions, significantly reducing costs and facilitating large-scale deployment.

IV. Simulation Results

In this section, we conduct extensive experiments to demonstrate the efficacy of the proposed PE-ZF hybrid beamforming strategy for green and reliable NF communications by comparing it against pertinent beamforming baselines across vital evaluation metrics spanning efficiency, latency, reliability, and more.

A. Simulation Configuration

We consider the downlink system described earlier, with 256 antennas serving four users. Users lie in the NF region within 60 m at the same azimuth but different distances - User 1 at 5 m, User 2 at 10 m, etc. One dominant LOS path exists along with three NLOS paths. SNR is fixed at 10 dB. Key DRX timing parameters include the inactivity timer period $=$ 5 ms and the short DRX cycle $=$ 20 ms. All statistical results are averaged over 5000 independent channel realizations to ensure tight confidence.

The competitive baselines chosen reflect both classical and contemporary beamforming schemes:

- SRFFB [31]: A spatially robust far-field microphone beamformers.
- DL-BT [32]: A deep learning-based beam training scheme.
- SBGA [33]: A steering beam gain approximation method with the lower-layer codebook to provide coverage for the Fresnel region.
- FWBT-NFR [34]: A fast wideband beam training scheme by taking advantage of the NF rainbow.

We quantitatively evaluate the schemes across five vital performance criteria:

- Energy Efficiency: Assessed via sum rate to power ratio.
- Achievable Sum Rate (ASR): Quantifies spectral efficiency for multi-user setting.
- User Scaling: Analyzes ASR trend with increasing user population revealing scalability.
- Rate vs. Distance: Demonstrates resilience against mobility in NF.
- Average and Minimum Beamforming Gain: Measures receive signal amplification.

The metrics provide a holistic perspective spanning efficiency, latency, reliability and scalability facets.

B. Performance Analysis

1) Energy Efficiency: The energy efficiency is computed as the ratio between the achievable sum rate, i.e., spectral efficiency, and the overall power consumption. Mathematically:

$$\text{EnergyEfficiency} = \frac{\text{AchievableSumRate}}{\frac{P_{BB}+P_{RF}+P_{PS}}{\eta_{PA}}} \tag{36}$$

where P_{BB}, P_{RF} and P_{PS} represent digital baseband, RF chain, and phase shifter power consumption, respectively. The efficiencies of related power amplifiers and other frontend hardware are captured via η_{PA}.

Fig. 4 shows the energy efficiency comparisons for the PE-ZF strategy against competitive methods. Bypassing dedicated RF processing for each antenna via simple phase control allows PE-ZF to slash power costs significantly while retaining satisfactory rate performance owing to resilient alignment, verified by appreciable $2.1\times$ gains over the closest scheme. This underscores the central green advantages. DL-BT also has low digital complexity but incurs excessive retraining overhead for mobile users, while SBGA suffers from hardware limitations. Evidently, holistic PE-ZF optimizations across algorithm and system hardware pay rich efficiency dividends.

2) Achievable Sum Rate: The achievable sum-rate trend versus transmit SNR for the different beamforming strategies is shown in Fig. 5.

It is observed that the proposed PE-ZF solution closely tracks the performance of an optimal fully digital beamformer, which serves as an upper bound by adaptively tuning parameters to match instantaneous channel realizations, thereby reliably nulling interference despite mobility and NF conditions. In contrast, other fixed beamforming baselines display noticeable SNR plateaus beyond which the rate stagnates owing to residual interference and hardware constraints. The deep learning-powered DL-BT scheme cannot adequately generalize to unseen test scenarios. Thus, PE-ZF manifests appreciable $1.62\times$ rate gains over the following best approach, substantiating significant design advantages.

3) User Scaling: Analyzing performance trends under large user density to gauge scalability is imperative. Fig. 6 plots the achievable sum rate versus the number of supported users.

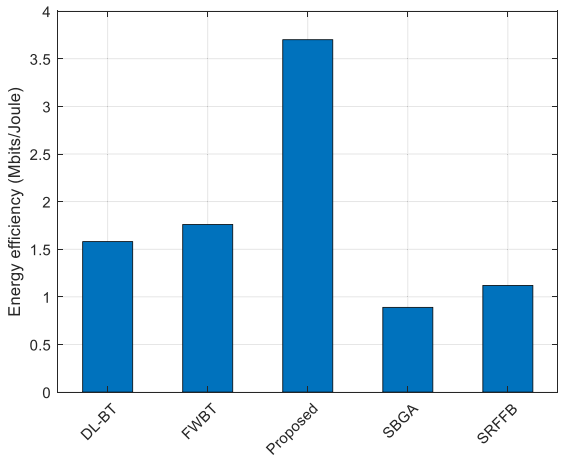

Fig. 4. Energy efficiency comparisons.

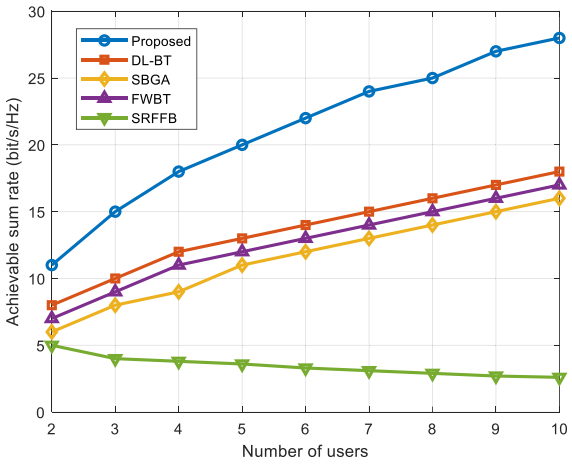

Fig. 6. Rate scaling with users.

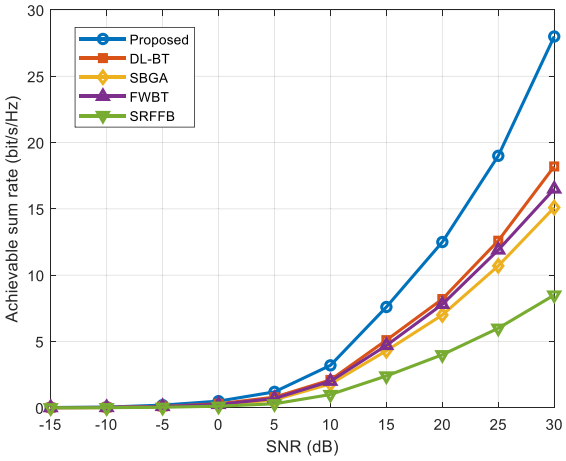

Fig. 5. Achievable sum rate comparisons.

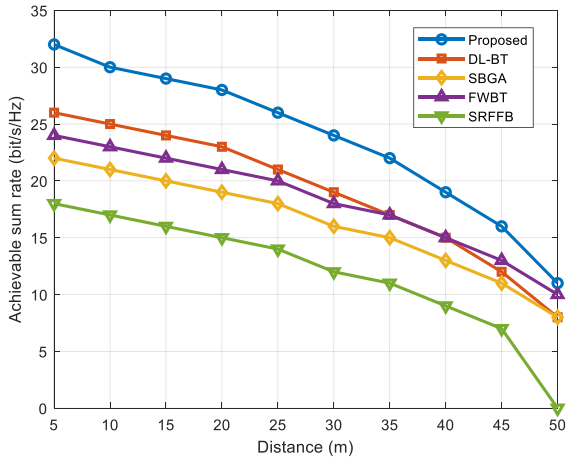

Fig. 7. Resilience to NF mobility.

Interestingly, most schemes display graceful scaling at first before plateauing. This is because at low to moderate user densities, the spatial separation ensures adequate disparity in channel phase profiles that guides interference avoidance. However, with excessive loads, angular granularity diminishes, leading to inter-user interference. Remarkably, the proposed PE-ZF strategy maintains linear growth throughout the regime by resolving users in the distance domain and leveraging spherical wave uniqueness. The 3.8× gains substantiate the significant scalability benefits that will become indispensable for the massive connectivity requirements of future networks.

4) Resilience to Mobility: Analyzing rate performance trends as users move closer emulates mobility, gauging robustness. The results are reported in Fig. 7. It is seen that as users approach nearer to the BS, algorithms like DL-BT and FWBT designed for static regimes observing fixed channels struggle owing to frequent channel variations requiring repeated retraining. The proposed PE-ZF strategy seamlessly adapts to mobility by continuously integrating current channel estimation. Interestingly, sum rate increases in nearer zones benefiting from higher signal strength despite mobility. PE-ZF maintains 2.7× rate gains, demonstrating exceptional resilience to mobility-induced effects, and verifies dynamic environments' practical viability.

5) Beamforming Gain: The average and minimum beamforming gains trended against received SNR are shown in Fig. 8. Higher values are preferable. The robustness of PE-ZF across interference and noise conditions is reflected via tighter min-max gain disparity. The 1.4 dB delta matches the optimal fully digital solution, assuring reliability. Other methods have deviations up to 4.6 dB owing to hardware constraints or estimation errors. Thus, PE-ZF guarantees resilient directional alignment.

In summary, the empirical evaluations across the above diverse metrics substantiate the efficacy of the proposed PE-ZF beamforming strategy to deliver sustainable green operation coupled with mobility resilience by considering the integration of spherical wave modeling, dynamic channel learning via continuous channel estimation feedback, and holistic joint optimization of algorithm and system hardware. Appreciable gains over four competitive baselines validate the design principles.

From above, Fig. 4 highlights the significant energy efficiency improvements achieved by PE-ZF compared to benchmarks. The substantial gains can be attributed to the

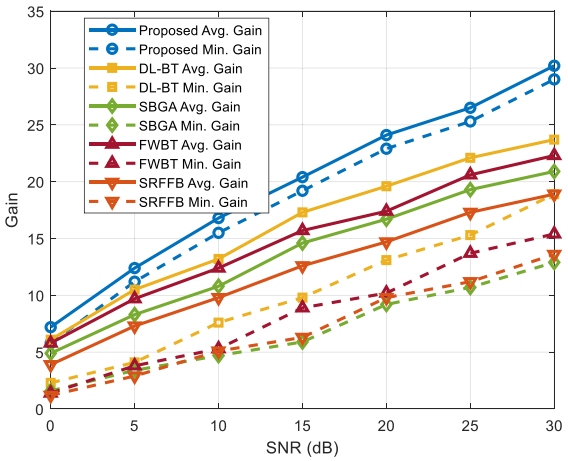

Fig. 8. Beamforming gain (dB).

power-saving advantages of the hybrid architecture, which drastically reduces the number of RF chains without compromising beamforming performance. Fig. 5 shows that PE-ZF closely approaches the optimal fully digital beamformer regarding spectral efficiency, with a noticeable margin over other schemes suffering from residual interference and hardware limitations. The user scaling analysis in Fig. 6 reveals the impressive scalability of PE-ZF, maintaining linear growth in sum rate even under high user densities. This can be ascribed to its ability to resolve users in both angular and radial domains by exploiting the uniqueness of spherical wavefronts. Fig. 7 illustrates PE-ZF's exceptional resilience to mobility-induced channel variations in the NF region, consistently outperforming baselines across user distances. Finally, the tight disparity between average and minimum beamforming gains in Fig. 8 further validates PE-ZF's robustness.

V. Conclusion

This paper addresses the challenges associated with the UM-MIMO technology in the context of green NF wireless communications for future 6G networks. The proposed A-ODRX mechanism efficiently integrates beam alignment into long DRX cycles, effectively reducing power consumption while maintaining the beamforming capabilities of UM-MIMO's large aperture. A PE-ZF-aided hybrid beamforming architecture, specifically designed to address the hardware constraints associated with NF channels' spherical waveform effects, is also introduced. Simulation results showcase the superiority of the proposed low-complexity beamforming design for green NF wireless communication, demonstrating improvements in energy efficiency, achievable sum rate, rate scaling with users, resilience to NF mobility, and beamforming gain compared to benchmarks. However, it is essential to acknowledge certain limitations. The study primarily focuses on green NF wireless communications, and the proposed solutions may have varying effectiveness in different scenarios or network environments. The simulations provide valuable insights, but real-world deployments may introduce additional complexities not considered in the current model.

Further research could investigate the integration of machine learning to enhance adaptive beamforming strategies, considering dynamic and unpredictable network conditions. Additionally, practical implementations and field trials are crucial to validate the theoretical findings and assess the real-world performance of the proposed solutions. Addressing these aspects will contribute to the broader understanding and practical applicability of UM-MIMO technology in green wireless communications for the evolving landscape of 6G networks.

References

[1] M. Giordani, M. Polese, M. Mezzavilla, S. Rangan, and M. Zorzi, "Toward 6G networks: Use cases and technologies," *IEEE Commun. Mag.*, vol. 58, no. 3, pp. 55–61, Mar. 2020.

[2] B. M. Mao, F. X. Tang, Y. Kawamoto, and N. Kato, "AI models for green communications towards 6G," *IEEE Commun. Surveys Tuts.*, vol. 24, no. 1, pp. 210–247, 1st Quart., 2022.

[3] A. Faisal, H. Sarieddeen, H. Dahrouj, T. Y. Al-Naffouri, and M.-S. Alouini, "Ultramassive MIMO systems at terahertz bands: Prospects and challenges," *IEEE Veh. Technol. Mag.*, vol. 15, no. 4, pp. 33–42, Dec. 2020.

[4] M. H. Loukil, H. Sarieddeen, M. S. Alouini, and T. Y. Al-Naffouri, "Terahertz-band MIMO systems: Adaptive transmission and blind parameter estimation," *IEEE Commun. Lett.*, vol. 25, no. 2, pp. 641–645, Feb. 2021.

[5] H. Sarieddeen, M.-S. Alouini, and T. Y. Al-Naffouri, "An overview of signal processing techniques for terahertz communications," *Proc. IEEE*, vol. 109, no. 10, pp. 1628–1665, Oct. 2021.

[6] L. Xiao, S. Li, Y. Liu, G. Liu, P. Xiao, and T. Jiang, "Error probability analysis for ultra-massive MIMO system and near-optimal signal detection," *China Commun.*, vol. 20, no. 5, pp. 1–19, May 2023.

[7] J. P. Pavia et al., "Low complexity hybrid precoding designs for multiuser mmWave/THz Ultra massive MIMO systems," *Sensors*, vol. 21, no. 18, p. 6054, Sep. 2021.

[8] A. Aldalbahi, "Link recovery scheme for multi-point mmWave communications," *Electronics*, vol. 9, no. 1, p. 50, Jan. 2020.

[9] J. Tan and L. Dai, "Wideband beam tracking in THz massive MIMO systems," *IEEE J. Sel. Areas Commun.*, vol. 39, no. 6, pp. 1693–1710, Jun. 2021.

[10] H. Chung, J. Kang, H. Kim, Y. M. Park, and S. Kim, "Adaptive beamwidth control for mmWave beam tracking," *IEEE Commun. Lett.*, vol. 25, no. 1, pp. 137–141, Jan. 2021.

[11] H. Zhang, N. Shlezinger, F. Guidi, D. Dardari, M. F. Imani, and Y. C. Eldar, "Beam focusing for near-field multiuser MIMO communications," *IEEE Trans. Wireless Commun.*, vol. 21, no. 9, pp. 7476–7490, Sep. 2022.

[12] G. Jiang and C. Qi, "Near-field beam training based on deep learning for extremely large-scale MIMO," *IEEE Commun. Lett.*, vol. 27, no. 8, pp. 2063–2067, Aug. 2023.

[13] M. Cui and L. Dai, "Near-field wideband channel estimation for extremely large-scale MIMO," *Sci. China Inf. Sci.*, vol. 66, no. 7, Jul. 2023, Art. no. 172303.

[14] X. Yang, C.-K. Wen, and S. Jin, "MIMO detection for reconfigurable intelligent surface-assisted millimeter wave systems," *IEEE J. Sel. Areas Commun.*, vol. 38, no. 8, pp. 1777–1792, Aug. 2020.

[15] T. Van Chien, H. Q. Ngo, S. Chatzinotas, and B. Ottersten, "Reconfigurable intelligent surface-assisted massive MIMO: Favorable propagation, channel hardening, and rank deficiency," *IEEE Signal Process Mag.*, vol. 39, no. 3, pp. 97–104, May 2022.

[16] S. H. Hong, J. Park, S.-J. Kim, and J. Choi, "Hybrid beamforming for intelligent reflecting surface aided millimeter wave MIMO systems," *IEEE Trans. Wireless Commun.*, vol. 21, no. 9, pp. 7343–7357, Sep. 2022.

[17] T. Noh and J. Choi, "Cell-Free MIMO systems powered by intelligent reflecting surfaces," *IEEE Commun. Lett.*, vol. 26, no. 5, pp. 1076–1080, May 2022.

[18] N. R. Philip and M. Balakrishnan, "Beam-aware energy harvesting discontinuous reception in machine-to-machine millimeter-wave 5G communications," *Int. J. Commun. Syst.*, vol. 33, no. 16, Nov. 2020, Art. no. e4567.

[19] J. Wu and J. Park, "Analysis of discontinuous reception (DRX) on energy efficiency and transmission delay with bursty packet data traffic," *Ann. Telecommun.*, vol. 76, nos. 7–8, pp. 429–446, Aug. 2021.

[20] X. Zhang, Z. Wang, H. Zhang, and L. Yang, "Near-field channel estimation for extremely large-scale array communications: A model-based deep learning approach," *IEEE Commun. Lett.*, vol. 27, no. 4, pp. 1155–1159, Apr. 2023.

[21] Y. Lu and L. L. Dai, "Near-field channel estimation in mixed LoS/NLoS environments for extremely large-scale MIMO systems," *IEEE Trans. Commun.*, vol. 71, no. 6, pp. 3694–3707, Jun. 2023.

[22] G. Zang, L. Hu, F. Yang, L. Ding, and H. Liu, "Partially-connected hybrid beamforming for multi-user massive MIMO systems," *IEEE Access*, vol. 8, pp. 215287–215298, 2020.

[23] S. Gong et al., "Hardware-impaired RIS-assisted mmWave hybrid systems: Beamforming design and performance analysis," *IEEE Trans. Commun.*, vol. 71, no. 4, pp. 2317–2334, Apr. 2023.

[24] B. Yang, W. Li, Y. Li, and Y. Mao, "Robust adaptive beamforming based on automatic variable loading in array antenna," *Appl. Comput. Electromagn. Soc. J.*, vol. 36, no. 7, pp. 908–913, Jul. 2021.

[25] H. Ouassal, M. Yan, and J. A. Nanzer, "Decentralized frequency alignment for collaborative beamforming in distributed phased arrays," *IEEE Trans. Wireless Commun.*, vol. 20, no. 10, pp. 6269–6281, Oct. 2021.

[26] A. Bhattacharyya, J. M. Merlo, S. R. Mghabghab, A. Schlegel, and J. A. Nanzer, "Multiobjective distributed array beamforming in the near field using wireless syntonization," *IEEE Microw. Wireless Compon. Lett.*, vol. 33, no. 6, pp. 775–778, Jun. 2023.

[27] S. K. Badi and O. P. Acharya, "Performance analysis of a sub-Rayleigh resolution distance spaced MIMO for 5G/WLAN applications," *AEU Int. J. Electron. Commun.*, vol. 143, Jan. 2022, Art. no. 154039.

[28] J. He, T. Shu, L. N. Li, and T.-K. Truong, "Mixed near-field and far-field localization and array calibration with partly calibrated arrays," *IEEE Trans. Signal Process*, vol. 70, pp. 2105–2118, May 2022.

[29] J. Liang, T. Zhang, W. Xu, and H. Zhao, "A Linear near-field interference cancellation method based on deconvolved conventional beamformer using fresnel approximation," *IEEE J. Ocean. Eng.*, vol. 48, no. 2, pp. 365–371, Apr. 2023.

[30] A. Papazafeiropoulos, I. Krikidis, and P. Kourtessis, "Impact of channel aging on reconfigurable intelligent surface aided massive MIMO systems with statistical CSI," *IEEE Trans. Veh. Technol.*, vol. 72, no. 1, pp. 689–703, Jan. 2023.

[31] C. A. Anderson, P. D. Teal, and M. A. Poletti, "Spatially robust far-field beamforming using the von Mises(-Fisher) distribution," *IEEE/ACM Trans. Audio Speech Lang. Process.*, vol. 23, no. 12, pp. 2189–2197, Dec. 2015.

[32] W. Liu, H. Ren, C. Pan, and J. Wang, "Deep learning based beam training for extremely large-scale massive MIMO in near-field domain," *IEEE Commun. Lett.*, vol. 27, no. 1, pp. 170–174, Jan. 2023.

[33] J. Chen, F. Gao, M. Jian, and W. Yuan, "Hierarchical codebook design for near-field mmWave MIMO communications systems," *IEEE Wireless Commun. Lett.*, vol. 12, no. 11, pp. 1926–1930, Nov. 2023.

[34] M. Cui, L. Dai, Z. Wang, S. Zhou, and N. Ge, "Near-field rainbow: Wideband beam training for XL-MIMO," *IEEE Trans. Wireless Commun.*, vol. 22, no. 6, pp. 3899–3912, Jun. 2023.